PHYSICAL REVIEW B **109**, 195129 (2024)

Comparative study of a high-entropy metal disulfide and its parent compounds using x-ray absorption spectroscopy

Anna Z. Laila,[1] Truc Ly Nguyen,[2] Ryota Furui,[1] Abhijeet Shelke,[2] Fan-Hsiu Chang,[2] Hong-Ji Lin,[2] Chien-Te Chen,[2]
Satoru Hamamoto,[3] Atsushi Fujimori,[2,4,5] Takashi Mizokawa,[6] Ashish Chainani,[2] and Ayako Yamamoto[1]
[1]*Graduate School of Engineering and Science, Shibaura Institute of Technology, Fukasaku 307, Saitama 337-8570, Japan*
[2]*National Synchrotron Radiation Research Center, Hsinchu 30076, Taiwan*
[3]*RIKEN SPring-8 Center, 1-1-1, Koto, Sayo-cho, Sayo-gun, Hyogo 679-5148, Japan*
[4]*Department of Physics, The University of Tokyo, 7-3-1 Hongo, Bunkyo-ku, Tokyo 113-0033, Japan*
[5]*Center for Quantum Science and Technology and Department of Physics, National Tsing Hua University, Hsinchu 30013, Taiwan*
[6]*Department of Applied Physics, Waseda University, Shinjuku, Tokyo 169-8555, Japan*

(Received 31 January 2024; revised 16 April 2024; accepted 17 April 2024; published 8 May 2024)

We study the local electronic structure of an equimolar-multimetal solid solution of high-entropy metal disulfide (Fe, Co, Ni, Cu)S_2 and its parent compounds MS_2 (M = Fe, Co, Ni, and Cu) using x-ray absorption spectroscopy (XAS). The Fe, Co, and Ni $L_{2,3}$-edge absorption spectra indicate a divalent metal state both in (Fe, Co, Ni, Cu)S_2 and its parent compounds, except for the Cu $L_{2,3}$-edge absorption spectra. The Cu $L_{2,3}$-edge spectra of CuS_2 and (Fe, Co, Ni, Cu)S_2 show satellites, which rule out the divalent Cu but can be analyzed as a combination of monovalent and trivalent copper states. The $L_{2,3}$-edge XAS spectral analysis with charge-transfer multiplet cluster model calculations was carried out for (Fe, Co, Ni, Cu)S_2 and its parent compounds. The estimated electronic parameters indicate a negative charge-transfer energy for the parent compounds and high-entropy compound (with the Ni L edge in the high-entropy compound being an exception), which corresponds to a p-p type lowest energy excitation in the extended Zaanen-Sawatzky-Allen phase diagram. The analysis shows that the charge-transfer energy Δ decreases and the on-site Coulomb energy U_{dd} increases systematically from Fe to Cu. The results suggest that in the high-entropy compound compared to the parent compounds, the hybridization strengths are weaker for Fe $3d$-S $3p$ and Co $3d$-S $3p$ and stronger for Ni $3d$-S $3p$ and Cu $3d$-S $3p$ bonds. This behavior is consistent with the longer Fe-S and Co-S bond distances and shorter Ni-S and Cu-S bond distances in the high-entropy compound compared to the parent compounds. The results indicate modifications in the structural lattice parameters of the high-entropy compound are reflected in the electronic structure and provides evidence for the so-called cocktail effect in the high-entropy compound.

DOI: 10.1103/PhysRevB.109.195129

I. INTRODUCTION

High-entropy alloys and compounds have attracted enormous attention in the last 20 years [1–10] and constitute a well-established field today. While early reports on metallic alloys with a large number of constituents in equal or near-equal proportions have discussed them in different ways such as "multicomponent alloys" [2,3], "multimaterial cocktails" [7], etc., the term "high-entropy alloys" was first used nearly 20 years ago [1]. In addition to alloys, the term "high-entropy" material is now used even for oxides [7], nitrides [8], sulfides [9], etc. While the original concept was to describe the properties of multicomponent materials in terms of their high configurational entropy [1,2], it is not necessarily valid for all multicomponent materials, because sometimes, they can exhibit a very small number of phases with wide solubility ranges [2]. Nonetheless, the salient features of multicomponent materials and high-entropy materials [1,2] are often discussed in terms of four principal features: (i) high-entropy effect, which lowers the free energy of solid solutions leading to their formation, especially at high temperatures, (ii) a sluggish diffusion effect, which happens because the neighboring atoms before and after a vacancy jump are different in such materials compared to conventional alloys, (iii) lattice distortion effect, which occurs because the strain energy increases due to size mismatch of neighboring atoms and affects properties, and (iv) the cocktail effect, which is a general term used to describe how properties of particular elements get modified and how component elements interact with neighboring atoms.

In this work, we carry out a study of the electronic states of a high-entropy metal disulfide (Fe, Co, Ni, Cu)S_2 that forms in the pyrite structure and compare it with its parent isostructural compounds FeS_2, CoS_2, NiS_2, and CuS_2, using x-ray absorption spectroscopy (XAS). The aim of this work is to investigate the changes in the electronic states of the high-entropy compound compared to individual parent compounds. Such a study is not easy to carry out in high-entropy transition metal alloys as the nearest neighbor of a transition metal is another transition metal atom. In order to simplify this problem, we decided to measure the XAS of a transition metal high-entropy compound because the spectra can be analyzed using model calculations. In particular, as is well known, core-level XAS and photoemission spectra can be modeled as a cluster consisting of a metal atom and nearest-neighbor ligands [11–13]. In the present case of metal disulfides forming in the pyrite structure, the XAS spectra can be calculated using an octahedral MS_6 cluster, where M is a transition metal and S is sulfur. Consequently, we can make a direct comparison of the XAS spectral shapes and their connection with electronic parameters obtained from the calculations for the parents as well as the high-entropy metal disulfide (Fe, Co, Ni, Cu)S_2. Such a comparative study of a high-entropy compound and its parents has not been reported to date and our attempt is to effectively check if there is any interplay between the so-called "lattice distortion effect" and the "cocktail effect," i.e., if there is an interplay of the modification of its crystal structure with electronic states and electronic parameters in the high-entropy compound compared to its parents.

XAS can provide us with the element-specific valence state, charge transfer between the transition metal and ligand, as well as the local electronic structure information of any material including high-entropy compounds. Further, XAS has the advantage that individual spectra can be analyzed in detail using charge-transfer multiplet cluster model calculations [12,13]. Comparison of experiments with calculations provides us with electronic parameters such as the crystal field splitting ($10Dq$), the charge-transfer energy (Δ), the d-d on-site Coulomb repulsion energy (U), and the hybridization strength ($pd\sigma$) between the metal element and ligands. Thus, it can allow us to describe the electronic structure of the parents and the high-entropy metal disulfide (Fe, Co, Ni, Cu)S_2. Such analyses can also possibly provide us with the origin of the physical and chemical property changes and the interplay between metal elements bridged by sulfur atoms in the high-entropy pyrite-type disulfide (Fe, Co, Ni, Cu)S_2.

Pyrite (FeS_2) is the most abundant mineral among sulfides with a simple cubic structure. The metal ions in the pyrite-type disulfides are formally considered divalent (M^{2+}) with a coordination number of six and residing in octahedral sites, while sulfur atoms form dimers (S_2^{2-}) with a coordination number of four in tetrahedral sites [14]. Pyrite-type disulfides can be synthesized under atmospheric as well as high-pressure conditions, except for CuS_2 and ZnS_2, which form only under high-pressure conditions [15]. Based on their ***d***-orbital configurations, these compounds have diverse magnetic and electronic properties, and here we focus on studying the parent $3d$ transition metal cation series for M = Fe to Cu and compare it with (Fe, Co, Ni, Cu)S_2 [16]. Briefly, it is known that FeS_2 shows a Fe^{2+} ion configuration ($d^6; t_{2g}^6 e_g^0$) with a band gap of $E_g = 0.9$ eV, and is reported to be a diamagnetic semiconductor [15]. CoS_2, with Co^{2+} ions ($d^7; t_{2g}^6 e_g^1$), is a metallic ferromagnet with a Curie temperature $T_c = 122$ K [17], and has been recently identified as a Weyl metal [18]. NiS_2 exhibits a Ni^{2+} ion configuration ($d^8; t_{2g}^6 e_g^2$) and is considered to be a strongly correlated antiferromagnetic insulator with a Néel temperature, $T_N = 39.2$ K [19]. CuS_2 with a Cu^{2+} ion ($d^9; t_{2g}^6 e_g^3$) is the only sulfide showing charge density wave order and superconductivity, but with a relatively low critical temperature $T_c = 1.50$ K [20,21] compared to the cuprate superconductors [22]. Several mixed two-cation pyrites have also been studied, and for example, $Ni_{1-x}Cu_xS_2$ shows paramagnetic metal behavior [23] while $Co_{1-x}Fe_xS_2$ exhibits half-metallic ferromagnetic ordering [24]. In the mixed pyrites case of $Co_{1-x}Fe_xS_2$, it was shown that the S-S bond distance remains nearly constant upon Fe substitution [24].

Recently, a few pyrite-based high-entropy materials have been reported that showed promising applications: (i) as an electrocatalyst [9,25] and (ii) as an electrode material in Li-ion batteries [26]. The low crystallinity and partially amorphous phase of (Fe, Ni, Co, Cr, M)S_2 (M = Mn, Cu, Zn, or Al) [9] behaved as an excellent electrocatalyst for oxygen evolution reaction (OER) activity with an exceptionally low overpotential of 199 and 308 mV at current densities of 10 and 1000 mA cm^{-2}, respectively. A high-performance electrocatalyst behavior for an OER with low overpotential and high current density was also reported for nanoparticles of (Co, Fe, Ni, Mn, Cu)S_2 [25]. Also, it was shown that high-entropy disulfides (Fe, Mn, Ni, M, M')S_2 (M, M' = Co, Ti, Cr, Cu) perform well as electrode materials for reversible electrochemical energy storage, showing high specific capacities and excellent rate capabilities in Li-ion batteries [26]. These samples were synthesized under atmospheric conditions at room temperature. Recently, we succeeded in synthesizing polycrystalline high-entropy metal disulfides (Fe, Co, Ni, Cu)S_2 and (Fe, Co, Ni, Cu, Ru)S_2 and studied their electrical and magnetic properties. These samples were stabilized using a high-pressure high-temperature (HP-HT) method using sealed capsules that have the advantages of prevention from high volatilization of sulfur, high reactivity, and a quick quenching process after sintering. In particular, we found that the HP-HT process is the key to forming an entropy-stabilized phase that yielded homogeneous and well-crystallized samples [27]. The (Fe, Co, Ni, Cu)S_2 and (Fe, Co, Ni, Cu, Ru)S_2 samples showed a ferrimagnetic ordering with T_c = 130 K in the soft magnetic category and metallic resistivity behavior.

The electronic structure of the parent pyrite-type compounds MS_2 have been studied by the methods of $2p$ core-level (or $L_{2,3}$-edge) photoemission spectroscopy [28] and XAS [29,30]. The metal $2p$ photoemission spectra analysis was done using cluster model calculations that yielded the electronic parameters that showed fair agreement with the experimental results on metal disulfides MS_2 with M = Fe to Ni [28]. On the other hand, the metal $L_{2,3}$-edge x-ray absorption spectral analysis of MS_2 with M = Fe to Ni was carried out using an atomic multiplet approach without charge-transfer states. The authors concluded that an increase in covalency results in an increase in the mixed character of the ground states and a charge-transfer model is required to model the spectra [29]. Further, an analysis of the $L_{2,3}$-edge absorption spectra using band structure calculations and molecular orbital calculations was also reported. The authors concluded that FeS_2, CoS_2, and NiS_2 exhibited a divalent M^{2+} state while CuS_2 was concluded to be a monovalent metal [30]. However, these calculations did not reproduce the experimentally observed atomic multiplet structure as well as the satellites in the XAS spectra, and the authors pointed out the importance of charge-transfer effects to model the spectra. In fact, CuS_2 has been studied for a long time but the question about its valency (Cu^{2+}, Cu^{1+}, or a mixture of Cu^{2+} and Cu^{1+}) and electronic structure continues to attract attention [31–36], mainly due to its unusual properties of low-T_c superconductivity ($T_c = 1.5$ K) and possible evidence for charge density wave order with $T_{\mathrm{CDW}} \sim 150$ K [20,21].

In this study, we attempt to elucidate the relation of the crystal structure and the local electronic structure of high-entropy metal disulfide (Fe, Co, Ni, Cu)S_2 and its parent compounds using the $L_{2,3}$-edge absorption spectra analysis with charge-transfer multiplet cluster model calculations. This corresponds to investigating the relation between the lattice distortion effect and the cocktail effect associated with electronic structure changes in the high-entropy metal disulfide compared to its parent compounds. The Fe, Co, and Ni $L_{2,3}$-edge absorption spectra indicate a divalent metal state both in (Fe, Co, Ni, Cu)S_2 and its parent compounds, while the Cu $L_{2,3}$-edge spectrum shows satellites and can be analyzed as a combination of monovalent and trivalent metal copper. The most suitable electronic parameters are obtained with a negative charge-transfer energy Δ for the parent compounds as well as the high-entropy compound, which indicates a *p-p* type lowest energy excitation in the Zaanen-Sawatzky-Allen (ZSA) phase diagram [37,38]. Only the Ni *L*-edge XAS of the high-entropy compound is an exception, as it requires a positive charge-transfer energy Δ. The electronic parameters obtained from the calculations indicate an evolution with the Δ decreasing while U increases systematically from Fe to Cu, as expected for the 3*d* transition metal series [28,37,39]. The results suggest that the hybridization strengths are weaker for Fe 3*d*-S 3*p* and Co 3*d*-S 3*p*, and stronger for Ni 3*d*-S 3*p* and Cu 3*d*-S 3*p* in the high-entropy compound, compared to the parent compounds. This allows us to make a correlation of the hybridization strengths with the longer Fe-S and Co-S bond distances and shorter Ni-S and Cu-S bond distances in the high-entropy compound.

II. EXPERIMENTAL DETAILS

The equimolar-multimetal high-entropy compound (Fe, Co, Ni, Cu)S_2 and its parent compounds, namely, FeS_2, CoS_2, NiS_2, and CuS_2 were synthesized as polycrystals using a cubic-anvil–type high-pressure high-temperature apparatus (Try Engineering, 180-ton press). The samples were prepared by mixing a powder of FeS, CoS, NiS, Cu_2S, and S, or Fe, Co, Ni, Cu, and S with a purity higher than 99%. The mixed powder was heated at high-pressure conditions of 2–4 GPa with two steps; prereaction at 500 °C for 30 min preventing from explosion by the gas of sulfur, and sintering at 900 °C for 30 min, then quenched within 5 s. This quenching process allowed us to obtain an entropy-stabilized phase. The crystal structure of all samples was adapted as a single phase of pyrite type collected by an x-ray diffractometer (Rigaku, SmartLab), and the lattice parameters were determined by the whole-pattern fitting method.

XAS measurements of (Fe, Co, Ni, Cu)S_2 and its parent compounds were carried out at the Dragon beamline 11 A of the Taiwan Light Source. The sample surfaces were scraped *in situ* by a diamond file in an ultrahigh-vacuum condition with pressures lower than 10^{-7} Pa to obtain clean surfaces at $T = 80$ K. The samples were cooled using a liquid-N_2 flow-type cryostat and the measurements were performed at a temperature of $T = 80$ K. The XAS data were measured in the total electron yield mode. Reference samples of Fe_2O_3, CoO, NiO, and Cu_2O were simultaneously measured at $T = 300$ K in a chamber positioned upstream and in-line with the main chamber to calibrate the photon energy. The O *K*-edge XAS spectral intensity from the sample surface for all the measurements was monitored and was less than 2% compared to the corresponding reference sample O *K*-edge spectra.

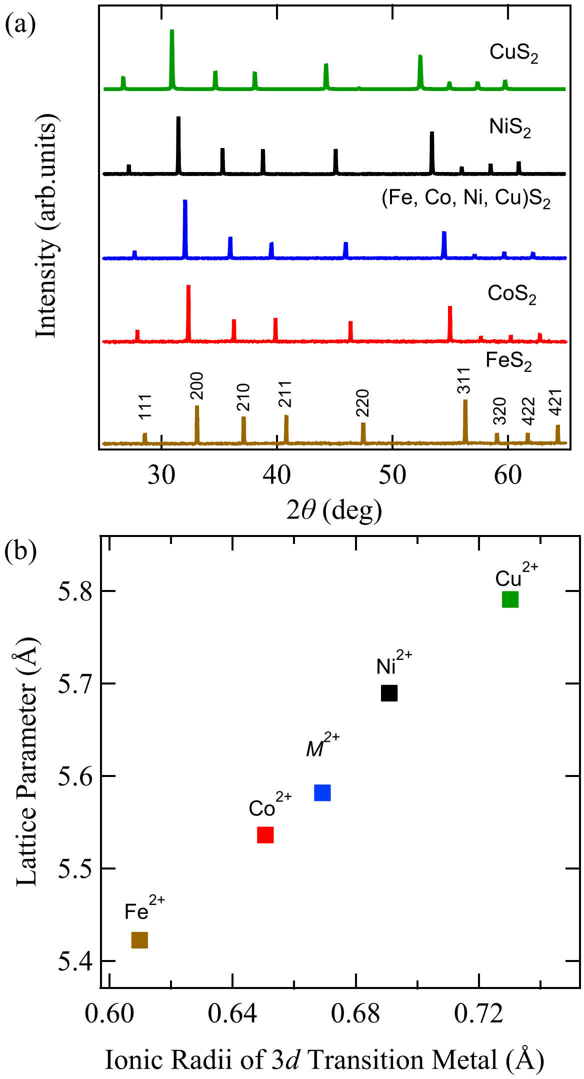

FIG. 1. (a) X-ray diffraction patterns of high-entropy metal disulfide (Fe, Co, Ni, Cu)S_2 and its parent compounds. (b) Lattice parameter *a* of high-entropy metal disulfide (Fe, Co, Ni, Cu)S_2 and its parent compounds plotted vs ionic radii of divalent six-coordinated 3*d* transition metal cations [40].

III. RESULTS

A. Structure analysis

Figure 1(a) shows powder x-ray diffraction patterns of the high-entropy metal disulfide (Fe, Co, Ni, Cu)S_2 and its parent compounds, indicating a single-phase simple cubic pyrite structure. The lattice parameter *a* of the parent compounds plotted as a function of the ionic radii [40] varies nearly linearly, from $a = 5.418(2)$ Å for FeS_2 to $a = 5.791(3)$ Å for CuS_2, as shown in Fig. 1(b). The equimolar solid solu-

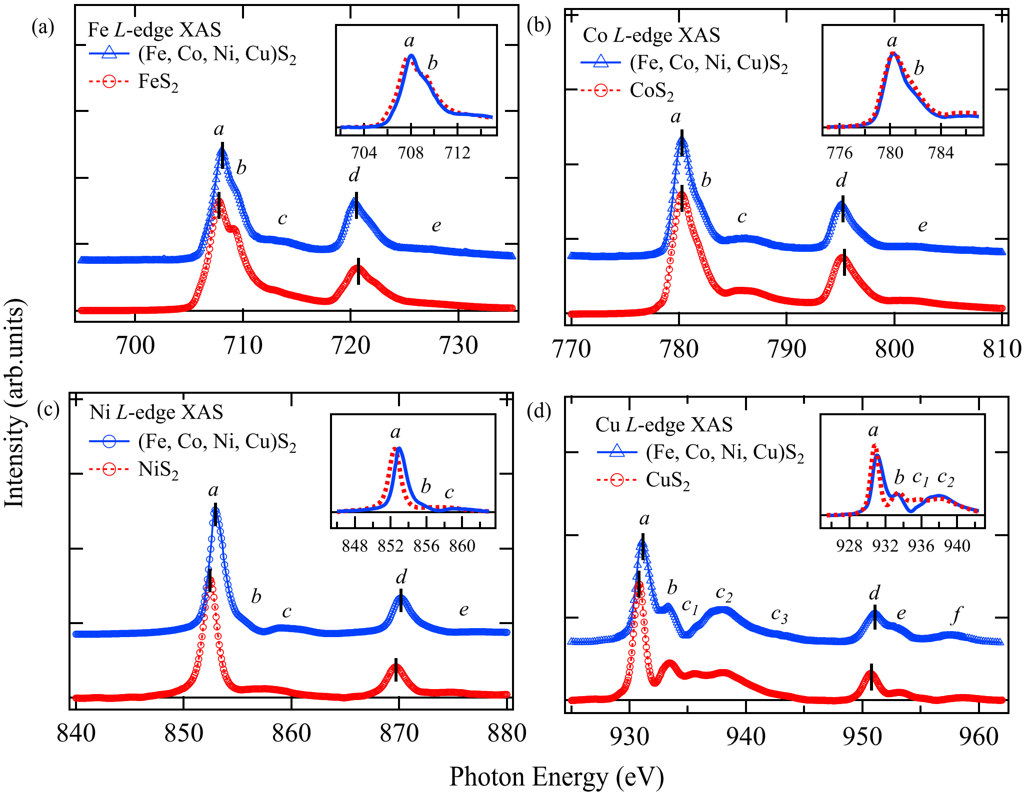

FIG. 2. Comparison of XAS L-edge experimental spectra of high-entropy metal disulfide (Fe, Co, Ni, Cu)S_2 with its parent compounds (a) FeS_2, (b) CoS_2, (c) NiS_2, and (d) CuS_2.

tion of the high-entropy compound (Fe, Co, Ni, Cu)S_2 shows a lattice parameter, $a = 5.583(12)$ Å, lying between CoS_2 and NiS_2. It can be understood that the high-entropy compound is expanded compared to FeS_2 and CoS_2 and compressed compared to NiS_2 and CuS_2. In a recent study, we discussed the qualitative relation between the lattice parameters and interatomic bonding in the high-entropy compound [27]. Given the isostructural behavior of all the samples, the lattice parameter differences suggest it should be possible to quantify and compare the metal $3d$-S $3p$ hybridization strengths in the samples, and we will discuss this later.

B. XAS of high-entropy metal disulfides and their parent compounds

Figure 2 shows the XAS L-edge experimental spectra of high-entropy metal disulfide (Fe, Co, Ni, Cu)S_2 with its parent compounds measured at $T = 80$ K. All the spectra shown in Fig. 2 have been normalized to the highest intensity main L_3-edge peaks, except for the Cu L-edge XAS of CuS_2 and (Fe, Co, Ni, Cu)S_2. The Cu L-edge XAS of CuS_2 and (Fe, Co, Ni, Cu)S_2 shows relatively larger changes in the satellite intensities and hence, they are plotted after normalizing for area under the curve. We also observed that the L_3- and L_2-edge main peaks of high-entropy pyrite (Fe, Co, Ni, Cu)S_2 tend to shift the higher photon energy compared to its parent compounds as the detail of shift photon energy can be seen at Table I. Figure 2(a) shows the Fe L-edge XAS of FeS_2 compared with that of (Fe, Co, Ni, Cu)S_2. It is seen that the Fe L_3-edge energy range of FeS_2 shows a main peak consisting of feature ***a*** at 707.8 eV photon energy consistent with an Fe^{2+} configuration, followed by a shoulder ***b*** at 709 eV and a weak broad satellite ***c*** spread between ∼712 and 714 eV. The Fe L_2-edge energy range shows a main peak feature ***d*** at ∼720.6 eV photon energy, followed by a very weak satellite ***e*** between ∼725 and 728 eV. In comparison, the Fe L_3 edge of (Fe, Co, Ni, Cu)S_2 shows a main peak feature ***a*** at a slightly higher photon energy of 708 eV, followed by a lower intensity shoulder ***b*** at 709 eV and a slightly higher intensity broad satellite ***c*** spread between ∼712 and 714 eV. The L_2-edge energy range shows a main peak feature ***d*** at ∼720.3 eV photon energy and a very weak satellite ***e*** between ∼725 and 728 eV.

In Fig. 2(b), we plot the Co L-edge XAS of CoS_2 and (Fe, Co, Ni, Cu)S_2. The Co L_3-edge energy range shows a

TABLE I. The L_3-edge and L_2-edge XAS main peak's energy positions of high-entropy metal disulfide (Fe, Co, Ni, Cu)S_2 and its parent compounds.

XAS	Compound	L_3-edge main peak (eV)	L_2-edge main peak (eV)
Fe L edge	FeS_2	707.8	720.3
	(Fe, Co, Ni, Cu)S_2	708.0	720.6
Co L edge	CoS_2	780.3	795.1
	(Fe, Co, Ni, Cu)S_2	780.3	795.2
Ni L edge	NiS_2	852.5	869.7
	(Fe, Co, Ni, Cu)S_2	852.8	870.2
Cu L edge	CuS_2	930.8	950.8
	(Fe, Co, Ni, Cu)S_2	931.1	951.1

main peak feature ***a*** at 780.3 eV photon energy confirming its Co^{2+} configuration, a weak shoulder ***b*** at 781 eV, which makes the main peak asymmetric, and a weak broad satellite ***c*** spread between ∼784 and 787 eV. The L_2-edge energy range shows a main peak feature ***d*** at ∼795.2 eV photon energy and a very weak satellite ***e*** between ∼800 and 803 eV. In comparison, the Co L_3-edge (Fe, Co, Ni, Cu)S_2 main peak feature ***a*** is at the same photon energy of 780.3 eV like CoS_2; the energy positions of shoulder ***b*** at 781 eV and the broad satellite ***c*** between ∼784 and 787 eV are also like CoS_2, but their intensities are lower compared to CoS_2. For example, the inset of Fig. 2(b) shows weaker intensity of the shoulder feature ***b*** of (Fe, Co, Ni, Cu)S_2 compared to CoS_2. The L_2-edge energy range shows a main peak feature ***d*** at ∼795.2 eV photon energy and a lower intensity satellite ***e*** between ∼800 and 803 eV, i.e., with energy positions quite close to CoS_2.

Figure 2(c) shows the Ni L-edge XAS of NiS_2 and (Fe, Co, Ni, Cu)S_2. The Ni L_3 edge of NiS_2 exhibits a main single-peak feature ***a*** at 852.5 eV photon energy, consistent with a Ni^{2+} configuration, and a weak broad satellite ***c*** spread between ∼856 and 860 eV. The Ni L_2 edge exhibits a main peak feature ***d*** at ∼869.7 eV photon energy and a very weak satellite ***e*** between ∼873 and 877 eV. In comparison, the Ni L_3 edge of (Fe, Co, Ni, Cu)S_2 shows a main peak feature ***a*** at a higher photon energy of 852.8 eV, a low intensity feature ***b*** at ∼854 eV, and a broad satellite ***c*** spread between ∼858 and 862 eV. The L_2 edge also shows a 0.3 eV shift for the main peak feature ***d*** at 870.2 eV photon energy and a very weak satellite ***e*** between ∼875 and 878 eV.

In Fig. 2(d), we plot the Cu L-edge XAS of CuS_2 and (Fe, Co, Ni, Cu)S_2 after normalizing to the area under the curve. The Cu L_3 edge of CuS_2 shows a main peak feature ***a*** at 930.8 eV photon energy and a well-separated small peak ***b*** at 933.4 eV. These two features have been discussed in the literature as originating from a Cu^{2+} and Cu^{1+} configuration, emphasizing the difficulty of a chemically stable pyrite phase of CuS_2 [29,30,33,34]. Interestingly, the Cu L_3 edge shows three additional satellites c_1, c_2, and c_3 spread between ∼935 and 945 eV, as labeled in Fig. 2(d). The Cu L_2 edge shows a main peak feature ***d*** at ∼950.8 eV photon energy, a weak peak ***e*** at ∼953.4 eV, and a weak broad satellite ***f*** between ∼955 and 962 eV. While similar satellites have been observed in CuS_2 XAS spectra earlier, surprisingly, their origin has not been discussed. This is mainly because only the Cu^{2+} and Cu^{1+} valence states corresponding to Cu d^9 and Cu d^{10} initial state configurations have been considered, respectively [41]. Using a cluster model for a Cu^{2+} d^9 initial state, the calculated Cu L-edge XAS spectrum can give rise to only a single-peak spectrum. This is because only one XAS final state is allowed for the Cu^{2+} d^9 initial state, corresponding to the $2p^63d^9 \rightarrow 2p^53d^{10}$ transition. Consequently, the L-edge $(2p - 3d)$ excitation can only lead to a single-peak feature for the Cu^{2+} initial state (as in CuO [41]) and cannot account for the satellite features. Further, for a Cu^{1+} initial state (as in Cu_2S), it was shown that the $L_{2,3}$ main peaks can be explained only in terms of a density of states picture, i.e., it is derived from hybridized states consisting of Cu 4s and 3d unoccupied states, which gives a small peak at about 933.4 eV and broad bump features up to 10 eV above the main peak [35], as is also seen in Cu_2O [41]. Based on the observed energies of the features for CuS_2, in the L_3 range, we assign feature ***b*** to the Cu^{1+} derived state. As we show in detail later in this work, by considering the possibility of Cu^{1+} and Cu^{3+} states, we can explain all features of the Cu L-edge XAS spectra. In particular, using the cluster model calculations as shown in Figs. 6 and 7, feature ***a*** mainly consists of a Cu^{3+} $(d^8) \rightarrow Cu^{1+}\underline{L}^2$ derived state. The satellite features $\boldsymbol{c_1}$ and $\boldsymbol{c_2}$ consist of a mixture of Cu^{1+} and Cu^{3+} derived states while satellite feature $\boldsymbol{c_3}$ is attributed to Cu^{1+} states. Similarly, in the L_2 range, feature ***e*** is assigned to Cu^{1+} states and feature ***d*** and satellite ***f*** are assigned to Cu^{3+}-derived states. Moving on to the Cu L_3 edge of (Fe, Co, Ni, Cu)S_2, the spectrum shows a broadened main peak feature ***a*** that is shifted to 931.1 eV photon energy and a well-separated small peak ***b*** at 933.4 eV. Interestingly, the relative intensity of peak ***a*** is reduced while peak ***b*** remains nearly the same as CuS_2 (see inset). The intensity of the satellite $\boldsymbol{c_1}$ is reduced while $\boldsymbol{c_2}$ and $\boldsymbol{c_3}$ spread between ∼935 and 945 eV remains nearly the same as CuS_2. The Cu L_2 edge shows a main peak feature ***d*** at ∼951.1 eV photon energy that is broadened and shifted, while peak ***e*** at ∼953 eV and the satellite ***f*** between ∼956 and 960 eV show very small differences compared to CuS_2. In the following, we analyze all the spectra using full atomic multiplet charge-transfer calculations.

C. Comparison of experimental XAS with cluster model calculated spectra

The Fe, Co, and Ni metal $L_{2,3}$-edge x-ray absorption analysis was carried out using a charge-transfer multiplet cluster model calculation using the CTM4XAS5.5 program [12,13]. The local MS_2 electronic states are approximated by a model consisting of an ML_6 cluster (where L is the ligand sulfur atoms in the present case) in octahedral (O_h) symmetry and uses the following electronic parameters to describe the initial state: the crystal field splitting $10Dq$, which is the bare energy separation between the e_g and t_{2g} orbitals, U_{dd} is the on-site d-d Coulomb repulsion energy, Δ is the charge-transfer energy between the $3d^n$ and $3d^{n+1}\underline{L}^1$ (where $\underline{L}^1$ corresponds to one hole in ligand states, and $(pd\sigma)$ is the metal 3d-S 3p hybridization strength [18]. However, for the Cu $L_{2,3}$-edge x-ray absorption analysis we used the CRISPY-QUANTY program [42,43] as we needed to consider three basis states ($3d^8$, $3d^9\underline{L}^1$, and $3d^{10}\underline{L}^2$) to suitably model the Cu^{3+} configuration. We also checked the Ni $L_{2,3}$-edge XAS calculation with three basis states but it was found to be very similar to the two-basis state calculations for the same parameters. For the final states, which correspond to exciting a 2p electron from the L edge to the unoccupied 3d states, an on-site core hole potential, U_{pd}, is included in addition to the above-described parameters. The calculation method is described in Refs. [12,13]. The calculated spectrum consists of all possible final states reached by the initial state and is obtained by convoluting the discrete states by broadening it with a Lorentzian function representing the lifetime and a Gaussian function representing the experimental resolution. The electronic parameters are varied to obtain a suitable match of the calculated spectra with the experimental spectra. XAS spectral calculations for the parent compounds FeS_2, CoS_2, NiS_2, CuS_2, and the

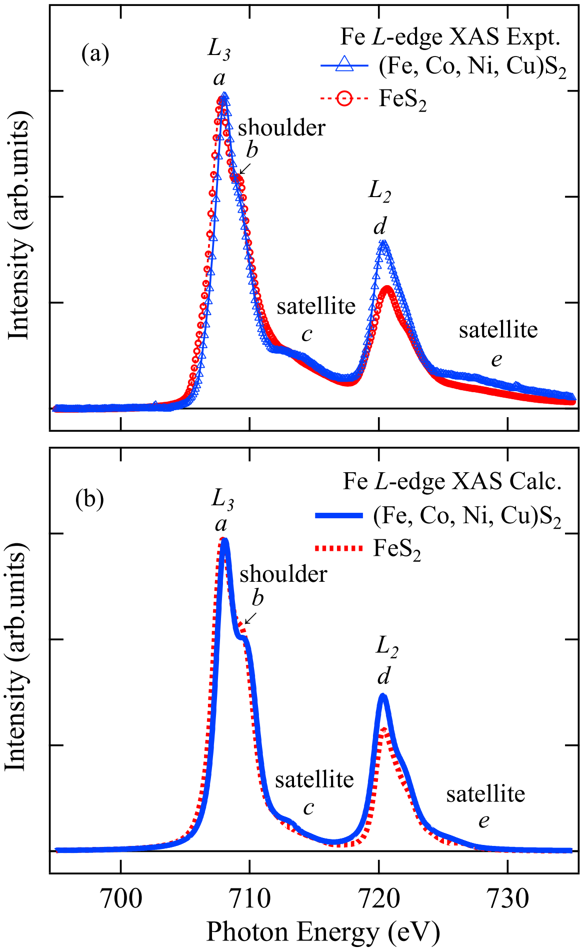

FIG. 3. (a) Experimental Fe *L*-edge XAS of high-entropy metal disulfide (Fe, Co, Ni, Cu)S$_2$ and its parent compound FeS$_2$. (b) The calculated Fe *L*-edge XAS describing the changes in high-entropy metal disulfide (Fe, Co, Ni, Cu)S$_2$ with a small increase in $10Dq$ and small reduction in hybridization strength ($pd\sigma$) compared to FeS$_2$, obtained using a full atomic multiplet charge-transfer cluster model.

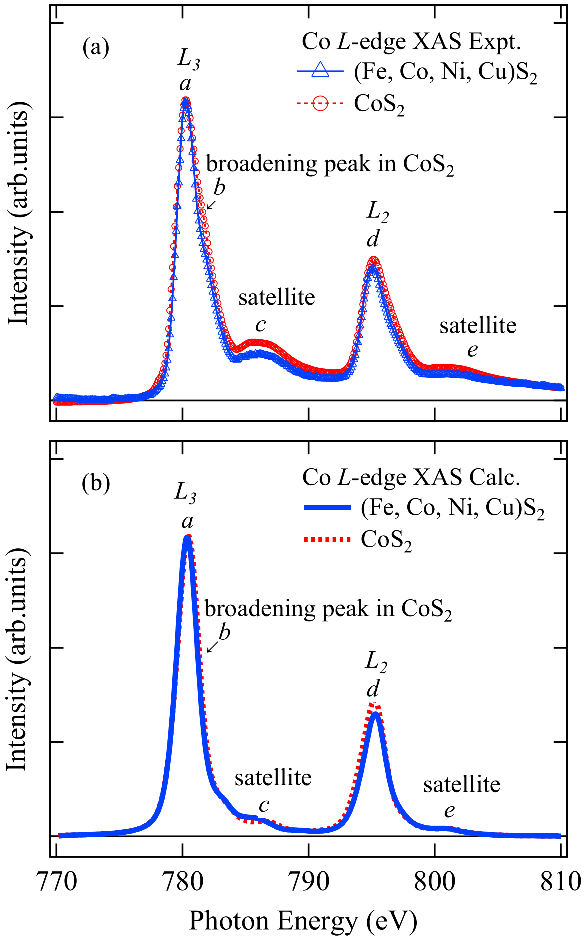

FIG. 4. (a) Experimental Co *L*-edge XAS of high-entropy metal disulfide (Fe, Co, Ni, Cu)S$_2$ and its parent compound CoS$_2$. (b) The calculated Co *L*-edge XAS describing the small changes in high-entropy metal disulfide (Fe, Co, Ni, Cu)S$_2$ are obtained by a small reduction in the hybridization strength ($pd\sigma$) compared to CoS$_2$.

high-entropy compound (Fe, Co, Ni, Cu)S$_2$ are shown in Figs. 3–6 for the Fe, Co, Ni, and Cu *L*-edge XAS results, respectively, comparing the parent and high-entropy compounds for each case. The obtained electronic parameters for the parents and the high-entropy compound are listed in Table II.

Figure 3(a) shows the experimental spectra of the Fe *L*-edge XAS of FeS$_2$ and (Fe, Co, Ni, Cu)S$_2$, plotted with the intensity normalized for the main peak. It can be seen from Fig. 3(b) that the spectral features for FeS$_2$ are suitably reproduced in the calculations. In particular, it is noted that the energy positions and intensities of the main peak, shoulder, and the satellite of the L_3 edge, as well as the main peak and weak satellite of the L_2 edge are well reproduced. The electronic parameters in Table II indicate that we need a negative charge-transfer energy $\Delta = -1.0$ eV and $U_{dd} = 4.5$ eV to obtain a suitable match of the calculated spectrum with the experimental spectrum. Further, in Fig. 3(b), it is also seen that for (Fe, Co, Ni, Cu)S$_2$, the energy positions and intensities of all the L_3-edge and L_2-edge features are reproduced by increasing $10Dq$ from 1.2 to 1.6 eV and reducing the hybridization strength ($pd\sigma$) from 1.4 to 1.3 eV, as listed in Table II.

In Fig. 4(a), we show the normalized experimental spectra of the Co *L*-edge XAS of CoS$_2$ and (Fe, Co, Ni, Cu)S$_2$. As seen in Fig. 4(b), we can reproduce the spectral features of the L_3 and L_2 edges suitably with the electronic parameters listed in Table II. In particular, Table II shows that for charge-transfer energy $\Delta = -1.5$ eV and $U_{dd} = 4.8$ eV, a suitable match between calculation and experiment is obtained for CoS$_2$, while for (Fe, Co, Ni, Cu)S$_2$, a reduction in hybridization strength ($pd\sigma$) from 2.0 to 1.8 eV with no other change in parameters results in reducing the main L_3 and L_2 peak widths by reducing the intensity of feature ***b*** at 781 eV, and also increases the satellite intensities a little as seen in experiment.

Next, we show the normalized experimental and calculated spectra of the Ni *L*-edge XAS of NiS$_2$ and (Fe, Co, Ni, Cu)S$_2$ in Figs. 5(a) and 5(b). The spectral features of the L_3 and L_2 edges of NiS$_2$ and (Fe, Co, Ni, Cu)S$_2$ can be reproduced by the electronic parameters as listed in Table II. While the large on-site Coulomb energy of $U_{dd} = 6.0$ eV is consistent with other Ni compounds including divalent NiO [11,36,44], the hybridization strength ($pd\sigma$) needs to be increased from

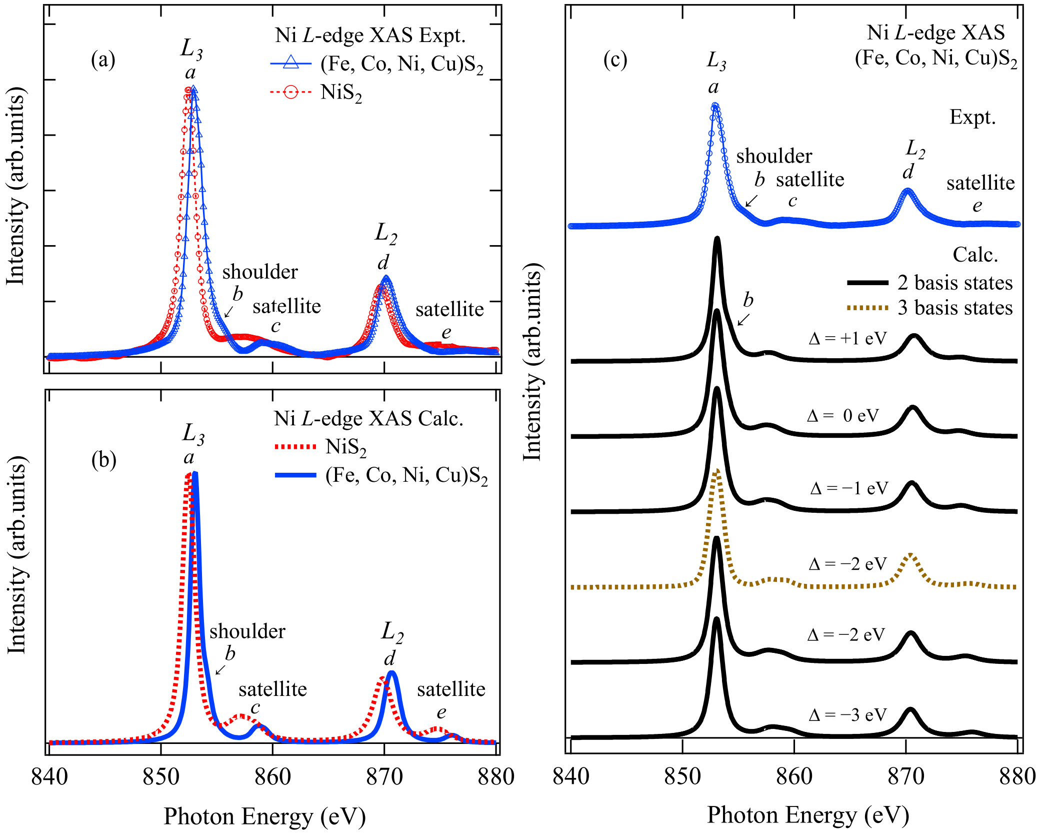

FIG. 5. (a) Experimental Ni L-edge XAS of high-entropy metal disulfide (Fe, Co, Ni, Cu)S_2 and its parent compound NiS_2. (b) The calculated Ni L-edge XAS describing the changes in high-entropy metal disulfide (Fe, Co, Ni, Cu)S_2 required a small positive charge-transfer energy Δ and higher hybridization strength ($pd\sigma$) compared to NiS_2, which is better described using a small negative charge-transfer energy Δ. (c) Comparison of Ni L-edge experimental XAS spectrum of high-entropy metal disulfide (Fe, Co, Ni, Cu)S_2 with calculations for different values of $\Delta = -3$ to $+1$ eV, in steps of 1 eV (keeping all other parameters fixed as for NiS_2), which shows that the shoulder (***b***) can be reproduced in the Ni L-edge XAS of high-entropy metal disulfide only with positive $\Delta = +1$ eV. Also shown in (c) is the comparison with the calculated spectra for negative $\Delta = -2.0$ eV using CTM4XAS with two basis states (black full line) and the CRISPY-QUANTY program with three basis states (brown dotted line).

2.0 eV for NiS_2 to 2.6 eV for (Fe, Co, Ni, Cu)S_2. The charge-transfer energy $\Delta = -2.0$ eV for NiS_2, and it follows the trend of becoming slightly more negative compared to the FeS_2 and CoS_2 parent compounds. It is noted that our Ni L-edge XAS of NiS_2 shows a single main peak and the weak satellite feature at higher photon energies is absent. On the other hand, an earlier study showed a weak satellite feature ***b***, and a relatively large positive charge-transfer energy of $\Delta = 5.0$ eV was required to reproduce the Ni L-edge XAS of NiS_2 [45]. However, our experimental and calculated XAS spectra are consistent with DFT+DMFT results reported by Kuneš *et al.* [46], which showed a p-p type gap in NiS_2 with the antibonding unoccupied $p_\sigma *$ band just above the Fermi level. Further, an important change is seen in the Ni L-edge XAS of metallic (Fe, Co, Ni, Cu)S_2. As shown in Fig. 5(a), the Ni L-edge XAS of (Fe, Co, Ni, Cu)S_2 exhibits a weak shoulder ***b*** at ~854 eV and leads to a small asymmetry just above the main peak. We first tried to reproduce the Ni L-edge XAS of (Fe, Co, Ni, Cu)S_2 using a negative Δ. In Fig. 5(c), we plot a set of spectra with different values of $\Delta = -3$ to $+1$ eV, in steps of 1 eV, keeping all other parameters fixed as for NiS_2. We also tried varying ($pd\sigma$) but could not reproduce the weak shoulder ***b*** at ~854 eV. In order to reproduce the weak shoulder ***b*** at ~854 eV in (Fe, Co, Ni, Cu)S_2, it was necessary to use a positive charge-transfer energy $\Delta = +1.0$ eV if we restrict the analysis to the single-site cluster model. It is noted that it may be possible also to reproduce the shoulder feature "b" by using a cluster model with more than one transition metal site as was done for NiO [47], but this calculation is beyond our scope. For NiS_2, it is also important to check whether the Ni L-edge XAS calculations with three basis states ($3d^8$, $3d^9\underline{L}^1$, and $3d^{10}\underline{L}^2$) show any remarkable difference compared to the two-basis states calculation shown in Fig. 5(b). In Fig. 5(c), we also plot the Ni L-edge XAS calculations with three basis states using the CRISPY-QUANTY program and the same parameters as for the calculation with two basis states shown in Fig. 5(b). As shown in Fig. 5(c), the results indicate that both the two- and the three-basis state calculations provide very similar Ni XAS spectra and confirm that the two-basis state calculations suffice to describe the Ni L-edge XAS of NiS_2.

It is interesting to note that the first spectroscopic validation of negative charge-transfer compounds also involved the electronic structure of a formally d^8 electron system, NaCuO_2 [38]. The behavior seen in the Ni L-edge XAS of NiS_2 is similar to the Cu L-edge XAS spectrum of NaCuO_2,

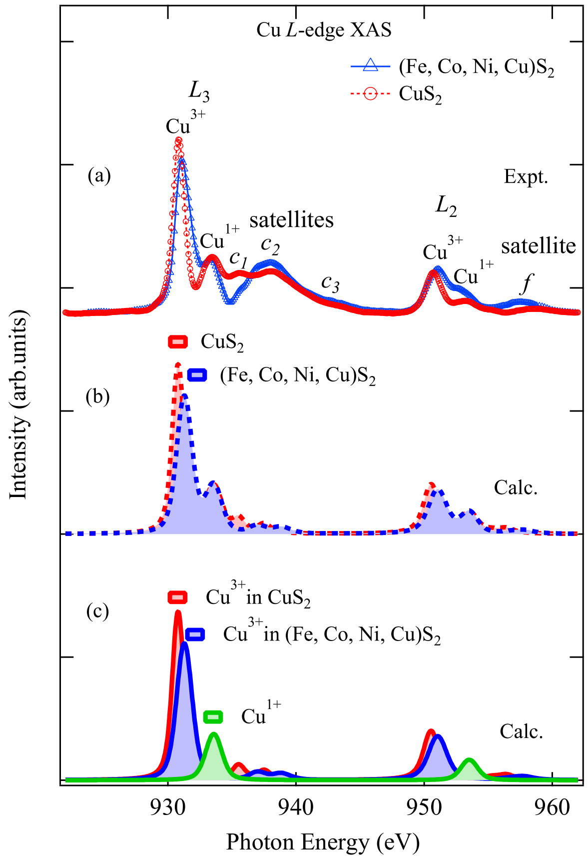

FIG. 6. (a) Experimental Cu L-edge XAS of CuS_2 and the high-entropy metal disulfide (Fe, Co, Ni, Cu)S_2. (b) Calculated Cu L-edge XAS of CuS_2 and the high-entropy metal disulfide (Fe, Co, Ni, Cu)S_2, obtained as a sum of the Cu^{1+}- and Cu^{3+}-derived spectra. In this case, we have used the sum of a single-peak Voigt function for the Cu^{1+} L_3 and L_2 features and full multiplet charge-transfer Cu^{3+} calculations to simulate the spectra. (c) shows the Cu^{1+} contribution (green curve) for both cases, while the Cu^{3+} contributions for CuS_2 and the high-entropy metal disulfide are shown as the red and blue curves, respectively.

which also exhibits a single main peak and was well simulated with a negative charge-transfer energy Δ [38]. It was shown that the band gap of $NaCuO_2$ corresponds to charge fluctuations mainly of the p-p type, with $d^{n+1}L^1 + d^{n+1}L^1 \rightarrow d^n + d^{n+2}L^2$, unlike the conventional Mott-Hubbard (d-d) type or the charge-transfer (p-d) type. Thus, the p-p type gap in NiS_2 is also like the p-p type gap of $NaCuO_2$. Further, as shown by Kuneš *et al.* [46], this insulating p-p type gap gets closed in the metal phase of $NiSe_2$. Such a metal-insulator transition is similar to the metal-insulator transition mechanism of negative-Δ compounds, as was pointed out for the insulating vs metallic behaviors of $NaCuO_2$ and $LaCuO_3$ [38,48], respectively. Here, for the metallic $LaCuO_3$, the leading peak in the Cu L-edge XAS is split into two peaks, demonstrating the breakdown of the single-site cluster model, as in the case of the Ni L-edge peak for the metallic (Fe,Co,Ni,Cu)S_2. The present results suggest a similar picture is the likely origin of the apparent significant change in charge-transfer energy Δ from -2 to $+1.0$ eV for describing the Ni L-edge XAS of insulating NiS_2 and metallic (Fe, Co, Ni, Cu)S_2, respectively, which is coupled to the increase in S-S distance and the decrease in the M-S distance, resulting in a small increase in the hybridization strength ($pd\sigma$) [27]. In fact, one must employ a multisite cluster model to reproduce the core-level spectra of $LaCuO_3$, as demonstrated by Okada and Kotani [49].

Figure 6 shows the normalized experimental and calculated spectra of the Cu L-edge XAS of CuS_2 and (Fe, Co, Ni, Cu)S_2. CuS_2 is known to show low-T_c superconductivity ($T_c = 1.5$ K) and has also been discussed to show evidence of charge density wave order [20,21]. As discussed in the Introduction, early studies of CuS_2 discussed the Cu L-edge XAS of CuS_2 in terms of a monovalent metal [30] but did not reproduce the experimentally observed atomic multiplet structure as well as the satellites in the XAS spectra. The authors pointed out the importance of charge-transfer effects to model the Cu L-edge XAS of CuS_2. Recently, it was shown by Streltsov *et al.* [50], that it is possible to discuss the electronic structure of gold ditelluride, $AuTe_2$, in terms of negative charge transfer. $AuTe_2$ is also a formally divalent material with Au^{2+} and Te_2^{2-}, as was shown by Ootsuki *et al.* [51]. Thus, $AuTe_2$ is considered to be like CuS_2 with Cu^{2+} and S_2^{2-}, and interestingly, it also exhibits low-T_c superconductivity like CuS_2. It was shown by Streltsov *et al.* [50] that $AuTe_2$ is a negative charge-transfer material, which can be described in terms of charge configurations as follows: $2Au^{2+}(d^9) \rightarrow Au^{1+}(d^{10}) + Au^{3+}(d^8)$, which can be written as $2Au^{2+} \equiv 2Au^{1+}\underline{L} \rightarrow Au^{1+} + Au^{1+}\underline{L}^2$, with two holes in the ligand $\underline{L}^2$ of the Te p band forming an antibonding state with the symmetry of a low-spin d^8 state of Au^{3+}.

If we apply the same picture to CuS_2, $2Cu^{2+}(d^9) \rightarrow Cu^{1+}(d^{10}) + Cu^{3+}(d^8)$, which can be written as

$$2Cu^{2+} \equiv 2Cu^{1+}\underline{L} \rightarrow Cu^{1+} + Cu^{1+}\underline{L}^2,$$

then the two holes in the ligand $\underline{L}^2$ of the S p band form an antibonding state (corresponding to the S_2^{2-} dimer), with the symmetry of a low-spin d^8 state of Cu^{3+}. It is interesting to note that a similar picture involving $2Ni^{3+} \equiv 2Ni^{2+}\underline{L} \rightarrow Ni^{2+} + Ni^{2+}\underline{L}^2$, was also used to discuss the charge ordering transition and metal-insulator transition in $NdNiO_3$ [52].

Based on this picture, to simulate the experimental spectra shown in Fig. 6(a), we have calculated the Cu L-edge XAS of CuS_2 and the high-entropy metal disulfide (Fe, Co, Ni, Cu)S_2 as a sum of Cu^{1+}- and Cu^{3+}-derived spectra. We first carried out full multiplet charge-transfer Cu^{3+} calculations with a negative charge transfer and the parameters are shown in Table II. Then, using a single-peak Voigt function to represent the Cu^{1+} contribution, the sum of Cu^{1+}- and Cu^{3+}-derived spectra was used to simulate the total spectra, as shown in Fig. 6(b). In Fig. 6(c), we plot the Cu^{1+} contribution (green curve) for both cases, while the Cu^{3+} contributions for CuS_2 and the high-entropy metal disulfide are shown as the red and blue curves, respectively. While this reproduces the main peaks ***a*** and ***b*** suitably, the relative intensity in the satellites c_1-c_3 is smaller than in the experimental data, indicating that the relative intensity of the Cu^{1+} states is significantly lower than the intensity of the Cu^{3+} states. However, if we subtract out the Cu^{3+} contribution from the total spectrum, as shown by the difference spectrum in Fig. 7(a), the spectral intensity at photon energies higher than peak ***a*** shows spectral weight

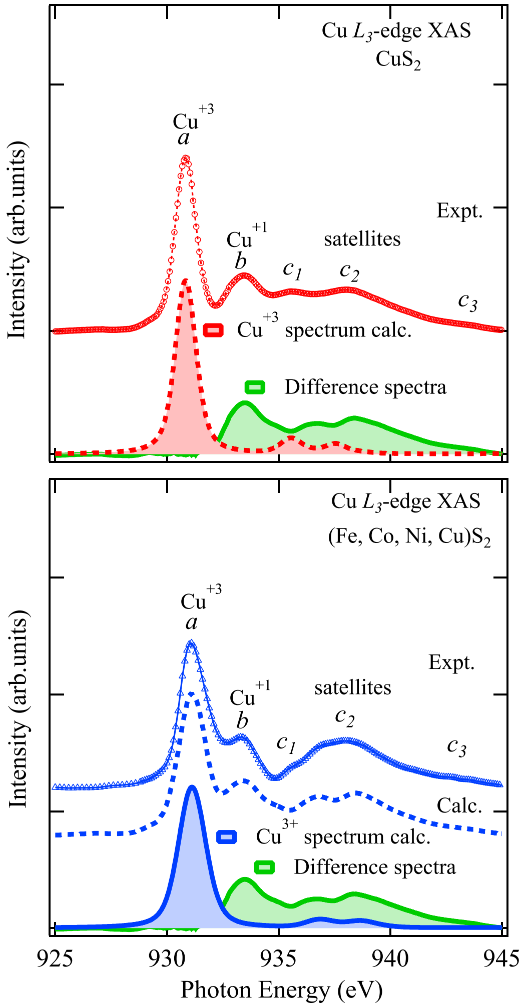

FIG. 7. (a) Experimental Cu L-edge XAS of CuS$_2$ together with the calculated Cu^{3+} spectrum (red curve) and the green curve shows the difference spectra obtained after subtracting the Cu^{3+} contribution at higher photon energies. (b) Experimental Cu L-edge XAS of the high-entropy metal disulfide (Fe, Co, Ni, Cu)S$_2$ together with the calculated Cu^{3+} spectrum (blue curve) and the green curve shows the difference spectra obtained after subtracting the Cu^{3+} contribution at higher photon energies.

nearly equal to the Cu^{3+} contribution, but spread over roughly 10 eV [green curve in Fig. 7(a)]. Further, the difference spectrum looks quite similar to the reported Cu$_2$S spectrum in the literature [29,34], which was suitably simulated in terms of hybridized Cu 4s and 3d density of states [30,35]. This suggests that the experimental spectra is best explained as a sum of the calculated charge-transferred Cu^{3+} states and Cu$_2$S-like Cu^{1+} states.

For the Cu L-edge XAS of the high-entropy metal disulfide (Fe, Co, Ni, Cu)S$_2$, surprisingly, if we just added the difference spectrum [green curve in Fig. 7(b)] representing the Cu$_2$S-like Cu^{1+} states to the calculated Cu^{3+} states [blue curve in Figs. 6(c) and 7(b)], with a slightly larger hybridization strength compared to the parent material [keeping all other electronic parameters fixed (see Table II)], we could suitably simulate the experimental spectrum as shown by dotted blue curve in Fig. 7(b). This suggests that the unoccupied states of the high-entropy metal disulfide (Fe, Co, Ni, Cu)S$_2$ mimic the unoccupied states of CuS$_2$ in the Cu L-edge XAS spectrum with small differences, although it must be noted that the high-entropy metal disulfide (Fe, Co, Ni, Cu)S$_2$ does not show superconductivity or charge density wave order down to 4 K. It is noted that for CuS$_2$, valence band photoemission spectroscopy studies also concluded a predominantly monovalent character with a fully occupied ***d*** band below the Fermi level and p-band character states near the Fermi level [33]. A recent density functional theory calculation of the electronic structure also concluded that the electronic structure for CuS$_2$ shows dominantly sulfur p states at and within 1 eV below and above the Fermi level [36]. Thus, the negative charge-transfer character ″p″-band metal or “anionic conductor” consistently explains the electronic structure of CuS$_2$ as probed by photoemission [33] as well as x-ray absorption spectroscopy.

IV. DISCUSSION

Overall, the electronic parameters listed in Table II indicate that there is a systematic evolution of the electronic structure parameters Δ and U_{dd} for the parent compounds. The charge-transfer energy Δ becomes increasingly more negative from Fe to Ni while it is the same for Ni and Cu. This trend is considered to be associated with the increasing electronegativity of 3d metal cations in the series from Fe to Cu. The only exception is the positive charge-transfer energy $\Delta = 1.0$ eV that is required for (Fe, Co, Ni, Cu)S$_2$ to reproduce the small shoulder feature at ~854 eV in (Fe, Co, Ni, Cu)S$_2$. On the other hand, U_{dd} increases systematically from Fe to Cu, which is well known, as the number of electrons n increases with d^n configuration [28,37,39]. It is noted that the crystal field energy 10Dq does not show systematic changes in the

TABLE II. The electronic parameters 10Dq, Δ, ($pd\sigma$), U_{dd}, and U_{pd} obtained from a full atomic multiplet charge-transfer cluster model.

XAS	Compound	10Dq +/–0.2 (eV)	$\Delta +/-0.5$ (eV)	$pd\sigma$ +/–0.2 (eV)	U_{dd} $+/-0.5$ (eV)	U_{pd} +/–0.5 (eV)
Fe L edge	FeS$_2$	1.2	−1.0	1.4	4.5	5.5
	(Fe, Co, Ni, Cu)S$_2$	1.6	−1.0	1.3	4.5	5.5
Co L edge	CoS$_2$	3.0	−1.5	2.0	4.8	6.0
	(Fe, Co, Ni, Cu)S$_2$	3.0	−1.5	1.8	4.8	6.0
Ni L edge	NiS$_2$	1.0	−2.0	2.0	6.0	7.0
	(Fe, Co, Ni, Cu)S$_2$	1.0	+1.0	2.6	6.0	7.0
Cu L edge	CuS$_2$	2.0	−2.0	2.0	6.0	7.5
	(Fe, Co, Ni, Cu)S$_2$	2.0	−2.0	2.6	6.0	7.5

parent and high-entropy compounds. In our analysis, the $10Dq$ does not change for the Co, Ni, and Cu L-edge absorption spectra (see Table II), but for the Fe L edge, it increases in the high-entropy compound compared to the parent compound, and suggests a more ionic picture for the Fe^{2+} states in the high-entropy compound with weaker $(pd\sigma)$ compared to FeS_2.

However, the most interesting behavior relevant to the properties of the high-entropy compound is the behavior of $(pd\sigma)$ in the parent compounds compared to the high-entropy compound. A careful look at the $(pd\sigma)$ values of the different metals hybridizing with sulfur ligands in the high-entropy compound with respect to the lattice parameter values suggests a direct correlation between crystal structure and the metal $3d$-anion $3p$ hybridization strength. The results suggest that the hybridization strengths for Fe $3d$-S $3p$ and Co $3d$-S $3p$ are weaker in the high-entropy compound compared to the parent compounds, as obtained in Table II. This is attributed to the lattice parameter of the high-entropy compound being larger than FeS_2 and CoS_2 [Fig. 1(b)]. In contrast, the hybridization strengths for Ni $3d$-S $3p$ and Cu $3d$-S $3p$ in the high-entropy compound are stronger compared to the parent compounds, because the lattice parameter of the high-entropy compound is smaller than NiS_2 and CuS_2, as obtained in our analysis. It is noted that for Ni and Cu L-edge XAS a shift to higher energy can be explained by a stronger $(pd\sigma)$ and shorter lattice parameters in the high-entropy compound. However, for Fe, the slightly weaker $(pd\sigma)$ in the high-entropy compound and larger lattice parameters does not explain the shift to a higher energy in the high-entropy compound and suggests that a change in $10Dq$ also plays a role in determining its energy. For Co, the nearly similar parameters for parent and high-entropy compounds with just a small reduction of 0.2 eV in $(pd\sigma)$, results in a negligible change of energy position in the high-entropy compound compared to the parent CoS_2.

Finally, it is important to discuss the electronic structure of the parent and high-entropy compounds in relation to the ZSA phase diagram [37]. It was shown by Zaanen *et al.* that in general, transition metal compounds fall into two main regimes, namely, the Mott-Hubbard (MH) region with $U < \Delta$ and the charge-transfer (CT) region with $U > \Delta$ [37], for positive values of Δ. In the MH region, the lowest energy excitation is a d-d excitation, while in the CT region, the lowest energy excitation is a p-d excitation. There is also another region associated with negative charge-transfer energy (negative-Δ) values. This region occurs in the extended ZSA phase diagram when the dominantly ligand character p-band crossing the Fermi level results in a split-off p state, and results in the lowest energy excitation to become a p-p excitation. It was pointed out in the ZSA phase diagram that metallic transition metal sulfides and selenides belong to this region with no gap in the p-p excitations and are effectively self-doped by holes. On the other hand, for insulating pyrites like NiS_2, the authors described that the ligand holes would be accommodated in the antibonding orbitals of sulfur pairs and form a band gap. This was explicitly shown to be the case based on DFT+DMFT studies reported recently for NiS_2 by Kuneš *et al.* [46]. In an independent study, using Born effective charge and density functional perturbation theory calculations, it was shown that FeS_2 can also be similarly described as a negative charge-transfer material with the antibonding state lying at the top of the valence band [53].

Several negative-Δ materials are now well known to occur for high valence states in oxides such as Cu^{3+} states in $NaCuO_2$ [38] and Ni^{3+} in $NdNiO_3$ [52]. In the present case of parent pyrite sulfides as well as the high-entropy compound, our results indicate that they are also well described as negative charge-transfer materials. Theoretical and experimental studies have also concluded that the series of parent compounds FeS_2, CoS_2, and NiS_2 [46,54,55] and also CuS_2 [33,36] exhibit significant anion ″p″ character states just below and above the Fermi level and are thus negative charge-transfer materials. While the insulating FeS_2 and NiS_2 can be described as materials showing a p-p gap, CoS_2 and CuS_2 exhibit metallic ground states, which can be described as p-band metallic materials self-doped by holes. In addition, for CuS_2, the obtained results showed the presence of Cu^{1+} and Cu^{3+} with negative charge transfer (Δ), thus suggesting that the charge density wave behavior of CuS_2 is likely associated with the ligand hole states. Further work is necessary to confirm this picture of a possible charge density wave transition in CuS_2. Interestingly, the behavior of Fe, Co, and Cu L-edge XAS in the high-entropy metal disulfide $(Fe, Co, Ni, Cu)S_2$ follows the same trend as the parent compounds with a negative charge-transfer energy, and only the Ni L-edge XAS indicates a positive charge-transfer energy.

V. CONCLUSIONS

In this study, we investigated the relation between the lattice distortion effect and the cocktail effect in the form of crystal structure changes coupled to the electronic structure of the high-entropy metal disulfide $(Fe, Co, Ni, Cu)S_2$. The $L_{2,3}$-edge XAS spectral analysis with full atomic multiplet charge-transfer cluster model calculations was carried out for $(Fe, Co, Ni, Cu)S_2$ and its parent compounds. The Fe, Co, and Ni $L_{2,3}$-edge absorption spectra indicate a divalent metal state both in $(Fe, Co, Ni, Cu)S_2$ and its parent compounds, while the Cu $L_{2,3}$-edge spectrum shows satellites, which can be analyzed as a combination of monovalent and trivalent copper states. The estimated electronic parameters for XAS spectra indicate a negative charge-transfer energy for the parent compounds and the high-entropy compound (with Ni L-edge XAS for the high-entropy compound being an exception), which corresponds to a p-$p$type lowest energy excitation in the extended Zaanen-Sawatzky-Allen phase diagram. The results indicate a systematic evolution with the Δ decreasing and U_{dd} increasing from Fe to Cu. The study suggests that in the high-entropy compound compared to the parent compounds, the hybridization strengths are weaker for the Fe $3d$-S $3p$ and Co $3d$-S $3p$ bonds and stronger for the Ni $3d$-S $3p$ and Cu $3d$-S $3p$ bonds. This behavior is consistent with the longer Fe-S and Co-S bond distances and the shorter Ni-S and Cu-S bond distances in the high-entropy compound compared to the parent compounds.

The authors are willing to share data with readers upon request, subject to data policies from respective institutions [Shibaura Institute of Technology (structural data); National Synchrotron Radiation Research Center (spectroscopy data)].

ACKNOWLEDGMENTS

This study was supported by Grant-in-Aid for Scientific Research, Japan, (Innovative Areas (Grants No. 760 18H05456 and No. 18H05462), Scientific Research (A) 761 (Grant No. 18H03692), and Scientific Research (C) (Grants 762 No. 20K05450 and No. 22K03535). Some of the measurements of physical properties were performed at CEMS, RIKEN, and Techno-plaza at Shibaura Institute of Technology. In addition, XAS measurements were conducted at beamline 11A National Synchrotron Radiation Research Center (NSRRC), Taiwan. A.C. thanks the National Science and Technology Council (NSTC) of the Republic of China, Taiwan for financially supporting this research under Contract No. NSTC 112-2112-M-213-031. A.F. acknowledges support from the Yushan Fellow Program under the Ministry of Education of Taiwan.

---

[1] J.-W. Yeh, S.-K. Chen, S.-J. Lin, J.-Y. Gan, T.-S. Chin, T.-T. Shun, C.-H. Tsau, and S.-Y. Chang, Nanostructured high entropy alloys with multiple principal elements: Novel alloy design concepts and outcomes, Adv. Eng. Mater. **6**, 299 (2004).

[2] B. Cantor, I. T. H. Chang, P. Knight, and A. J. B. Vincent, Microstructure development in equiatomic multicomponent alloys, Mater. Sci. Eng., A **213** 375 (2004).

[3] B. Cantor, K. B. Kim, and P. J. Warren, Novel multicomponent amorphous alloys, Mater. Sci. Forum **386**, 27 (2002).

[4] S. Ranganathan, Alloyed pleasures: Multimetallic cocktails, Curr. Sci. **85**, 1404 (2003).

[5] B. Cantor, Multicomponent and high entropy alloys, Entropy **16**, 4749 (2014).

[6] M.-H. Tsai, Physical properties of high entropy alloys, Entropy **15**, 5338 (2013).

[7] C. M. Rost, E. Sachet, T. Borman, A. Moballegh, E. C. Dickey, D. Hou, J. L. Jones, S. Curtarolo, and J.-P. Maria, Entropy-stabilized oxides, Nat. Commun. **6**, 8485 (2015).

[8] C.-H. Tsau and Y.-H. Chang, Microstructures and mechanical properties of $TiCrZrNbN_x$ alloy nitride thin films, Entropy **15**, 5012 (2013).

[9] T. X. Nguyen, Y. H. Su, C. C. Lin, and J. M. Ting, Self-reconstruction of sulfate-containing high entropy sulfide for exceptionally high-performance oxygen evolution reaction electrocatalyst, Adv. Funct. Mater. **31**, 2106229 (2021).

[10] D. B. Miracle and O. N. Senkov, A critical review of high entropy alloys and related concepts, Acta Mater. **122**, 448 (2017).

[11] G. van der Laan, J. Zaanen, G. A. Sawatzky, R. Karnatak, and J.-M. Esteva, Comparison of x-ray absorption with x-ray photoemission of nickel dihalides and NiO, Phys. Rev. B **33**, 4253 (1986).

[12] F. M. F. de Groot, X-ray absorption and dichroism of transition metals and their compounds, J. Electron Spectrosc. Relat. Phenom. **67**, 529 (1994).

[13] E. Stavitski and F. M. F. de Groot, The CTM4XAS program for EELS and XAS spectral shape analysis of transition metal L-edges, Micron **41**, 687 (2010).

[14] C. Arrouvel and J. G. Eon, Understanding the surfaces and crystal growth of pyrite FeS_2, Mater. Res. **22**, e20171140 (2019).

[15] T. A. Bither, R. J. Bouchard, W. H. Cloud, P. C. Donohue, and W. J. Siemons, Transition metal pyrite dichalcogenides. High-pressure synthesis and correlation of properties, Inorg. Chem. **7**, 2208 (1968).

[16] W. M. Temmerman, P. J. Durham, and D. J. Vaughan, The electronic structures of the pyrite-type disulphides (MS_2, where M = Mn, Fe, Co, Ni, Cu, Zn) and the bulk properties of pyrite from local density approximation (LDA) band structures calculations, Phys. Chem. Minerals **20**, 248 (1993).

[17] A. Teruya, F. Suzuki, D. Aoki, F. Honda, A. Nakamura, M. Nakashima, Y. Amako, H. Harima, K. Uchima, M. Hedo, T. Nakama, and Y. Ōnuki, Fermi surface and magnetic properties in ferromagnet CoS_2 and paramagnet $CoSe_2$ with the pyrite-type cubic structure, J. Phys.: Conf. Ser. **807**, 012001 (2017).

[18] N. B. M. Schröter, I. Robredo, S. Klemenz, R. J. Kirby, J. A. Krieger, D. Pei, T. Yu, S. Stolz, T. Schmitt, P. Dudin, and T. Weyl fermions, Fermi arcs, and minority-spin carriers in ferromagnetic CoS_2, Sci. Adv. **6**, eabd5000 (2020).

[19] T. Higo and S. Nakatsuji, Magnetization anomaly due to the non-coplanar spin structure in NiS_2, J. Phys. Soc. Jpn. **84**, 053702 (2015).

[20] Y. Takano, N. Uchiyama, S. Ogawa, N. Mori, Y. Kimishima, S. Arisawa, A. Ishii, T. Hatano, and K. Togano, Superconducting properties of $CuS_{2-x}Se_x$, under high pressure, Phys. C (Amsterdam, Neth.) **341**, 739 (2000).

[21] M. Kakihana, T. D. Matsuda, R. Higashinaka, Y. Aoki, A. Nakamura, D. Aoki, H. Harima, M. Hedo, T. Nakama, and Y. Onuki, Superconducting and Fermi surface properties of pyrite-type compounds CuS_2 and $CuSe_2$, J. Phys. Soc. Jpn. **88**, 014702 (2019).

[22] A. Yamamoto, N. Takeshita, C. Terakura, and Y. Tokura, High pressure effects revisited for the cuprate superconductor family with highest critical temperature, Nat. Commun. **6**, 8990 (2015).

[23] A. Maignan, R. Daou, E. Guilmeau, D. Berthebaud, T. Barbier, O. Lebedev, and S. Hébert, Thermoelectric properties, metal-insulator transition, and magnetism: Revisiting the $Ni_{1-x}Cu_xS_2$ system, Phys. Rev. Mater. **3**, 115401 (2019).

[24] K. Ramesha, R. Seshadri, C. Ederer, T. He, and M. A. Subramanian, Experimental and computational investigation of structure and magnetism in pyrite $Co_{1-x}Fe_xS_2$: Chemical bonding and half-metallicity, Phys. Rev. B **70**, 214409 (2004).

[25] M. Moradi, F. Hasanvandian, A. Bahadoran, A. Shokri, S. Zerangnasrabad, and B. Kakavandi, New high-entropy transition-metal sulfide nanoparticles for electrochemical oxygen evolution reaction, Electrochim. Acta **436**, 141444 (2022).

[26] L. Lin, K. Wang, A. Sarkar, C. Njel, G. Karkera, Q. Wang, R. Azmi, M. Fichtner, H. Hahn, S. Schweidler, and B. Breitung, High-entropy sulfides as electrode materials for Li-ion batteries, Adv. Energy, Mater. **12**, 2103090 (2022).

[27] A. Z. Laila, M. Fronzi, S. Kumegai, K. Sugiyama, R. Furui, and A. Yamamoto, High-pressure synthesis of high-entropy metal disulfides with pyrite-type structure, J. Phys. Soc. Jpn. **91**, 084802 (2022).

[28] A. E. Bocquet, T. Mizokawa, T. Saitoh, H. Namatame, and A. Fujimori, Electronic structure of $3d$-transition-metal compounds by analysis of the $2p$ core-level photoemission spectra, Phys. Rev. B **46**, 3771 (1992).

[29] J. M. Charnock, C. M. B. Henderson, J. F. W. Mosselmans, and R. A. D. Pattrick, 3d transition metal L-edge X-ray absorption studies of the dichalcogenides of Fe, Co, and Ni, Phys. Chem. Minerals **23**, 403 (1996).

[30] J. F. W. Mosselmans, R. A. D. Pattrick, G. Van Der Laan, J. M. Charnock, D. J. Vaughan, C. M. B. Henderson, and C. D. Garner, X-ray absorption near-edge spectra of transition metal disulfides FeS_2 (pyrite and marcasite), CoS_2, NiS_2, and CuS_2, and their isomorphs FeAsS and CoAsS, Phys. Chem. Minerals **22**, 311 (1995).

[31] H. E. King, Jr. and C. T. Prewitt, Structure and symmetry of CuS_2 (pyrite structure), Am. Mineral. **64**, 1265 (1979).

[32] A. Fujimori, K. Mamiya, T. Mizokawa, T. Miyadai, T. Sekiguchi, H. Takahashi, N. Mori, and S. Suga, Resonant photoemission study of pyrite-type NiS_2, CoS_2, and FeS_2, Phys. Rev. B **54**, 16329 (1996).

[33] H. Ueda, M. Nohara, K. Kitazawa, H. Takagi, A. Fujimori, T. Mizokawa, and T. Yagi, Copper pyrites CuS_2 and $CuSe_2$ as anion conductors, Phys. Rev. B **65**, 155104 (2002).

[34] S. W. Goh, A. N. Buckley, and R. N. Lamb, Copper(II) sulfide? Miner. Eng. **19**, 204 (2006).

[35] J. R. Vegelius, K. O. Kvashnina, H. Hollmark, M. Klintenberg, Y. O. Kvashnin, I. L. Soroka, L. Werme, and S. M. Butorin, X-ray spectroscopic study of Cu_2S, CuS, and copper films exposed to Na_2S solutions, J. Phys. Chem. C **116**, 22293 (2012).

[36] Y. Yin, J. Coulter, C. J. Ciccarino, and P. Narang, Theoretical investigation of charge density wave instability in CuS_2, Phys. Rev. Mater. **4**, 104001 (2020).

[37] J. Zaanen, G. A. Sawatzky, and J. W. Allen, Band gaps and electronic structure of transition metal compounds, Phys. Rev. Lett. **55**, 418 (1985).

[38] T. Mizokawa, H. Namatame, A. Fujimori, K. Akeyama, H. Kondoh, H. Kuroda, and N. Kosugi, Origin of the band gap in the negative charge-transfer-energy compound $NaCuO_2$, Phys. Rev. Lett. **67**, 1638 (1991); T. Mizokawa, A. Fujimori, H. Namatame, K. Akeyama, and N. Kosugi, Electronic structure of the local-singlet insulator $NaCuO_2$, Phys. Rev. B **49**, 7193 (1994).

[39] T. Bandyopadhyay and D. D. Sarma, Calculation of Coulomb interaction strengths for $3d$ transition metals and actinides, Phys. Rev. B **39**, 3517 (1989).

[40] R. D. Shannon, Revised effective ionic radii and systematic studies of interatomic distances in halides and chalcogenides, Acta Crystallogr., Sect. A: Found Adv. **32**, 751 (1976).

[41] M. Grioni, J. F. van Acker, M. T. Czyzyk, and J. C. Fuggle, Unoccupied electronic structure and core-hole effects in the x-ray-absorption spectra of Cu_2O, Phys. Rev. B **45**, 3309 (1992).

[42] M. W. Haverkort, M. Zwierzycki, and O. K. Andersen, Multiplet ligand-field theory using Wannier orbitals, Phys. Rev. B **85**, 165113 (2012).

[43] M. Retegan, Crispy: version 0.7.3, https://github.com/mretegan/crispy, 2019.

[44] A. Fujimori and F. Minami, Valence-band photoemission and optical absorption in nickel compounds, Phys. Rev. B **30**, 957 (1984).

[45] J. Jeong, K. Park, E. Cho, H. Noh, S. Kim, and H. Kim, Electronic structure change of $Ni_{2-x}Se_x$ in the metal-insulator transition probed by x-ray absorption spectroscopy, J. Korean Phys. Soc. **72**, 111 (2018).

[46] J. Kuneš, L. Baldassarre, B. Schächner, K. Rabia, C. A. Kuntscher, Dm. M. Korotin, V. I. Anisimov, J. A. McLeod, E. Z. Kurmaev, and A. Moewes, Metal-insulator transition in $NiS_{2-x}Se_x$, Phys. Rev. B **81**, 035122 (2010).

[47] M. A. Veenendaal and G. A. Sawatzky, Nonlocal screening effects in $2p$ x-ray photoemission spectroscopy core-level line shapes of transition metal compounds, Phys. Rev. Lett. **70**, 2459 (1993).

[48] T. Mizokawa, A. Fujimori, H. Namatame, Y. Takeda, and M. Takano, Electronic structure of tetragonal $LaCuO_3$ studied by photoemission and x-ray-absorption spectroscopy, Phys. Rev. B **57**, 9550 (1998).

[49] K. Okada and A. Kotani, Large cluster effects on core-level photoabsorption spectrum of $LaCuO_3$, J. Phys. Soc. Jpn. **68**, 666 (1999).

[50] S. V. Streltsov, V. V. Roizen, A. V. Ushakov, A. R. Oganov, and D. I. Khomskii, Old puzzle of incommensurate crystal structure of calaverite $AuTe_2$ and predicted stability of novel AuTe compound, Proc. Natl Acad. Sci. USA **115**, 9945 (2018).

[51] D. Ootsuki, K. Takubo, K. Kudo, H. Ishii, M. Nohara, N. L. Saini, R. Sutarto, F. He, T. Z. Regier, M. Zonno, M. Schneider, G. Levy, G. A. Sawatzky, A. Damascelli, and T. Mizokawa, Effect of Pt substitution on the electronic structure of $AuTe_2$, Phys. Rev. B **90**, 144515 (2014).

[52] V. Bisogni, S. Catalano, R. J. Green, M. Gibert, Y. Huang, R. Scherwitzl, V. N. Strocov, P. Zubko, S. Balandeh, J.-M. Triscone, G. Sawatzky, and T. Schmitt, Ground-state oxygen holes and the metal-insulator transition in the negative charge-transfer rare-earth nickelates, Nat. Commun. **7**, 13017 (2016).

[53] N. A. Pike, B. Van Troeye, A. Dewandre, G. Petretto, X. Gonze, G. M. Rignanese, and M. J. Verstraete, Origin of the counterintuitive dynamic charge in the transition metal dichalcogenides, Phys. Rev. B **95**, 201106(R) (2017).

[54] W. Folkerts, G. A. Sawatzky, C. Haas, R. A. de Groot, and F. U. Hillebrecht, Electronic structure of some 3D transition-metal pyrites, J. Phys. C: Solid State Phys. **20**, 4135 (1987).

[55] E. Pavarini, E. Koch, J. van den Brink, and G. Sawatzky, *Quantum Materials: Experiments and Theory* (Verlag des Forschungszentrum Jülich, Jülich, 2016), Chap. 1, p. 18.